Urolithiasis and hepatotoxicity are linked to the anion transporter Sat1 in mice

Paul A. Dawson,[1] Christopher S. Russell,[2] Soohyun Lee,[1] Sarah C. McLeay,[1] Jacobus M. van Dongen,[3] David M. Cowley,[3] Lorne A. Clarke,[2] and Daniel Markovich[1]

[1]School of Biomedical Sciences, University of Queensland, Brisbane, Australia. [2]Department of Medical Genetics and the Child and Family Research Institute, University Of British Columbia, Vancouver, Canada. [3]Pathology Department, Mater Misercordiae Hospital, South Brisbane, Australia.

Urolithiasis, a condition in which stones are present in the urinary system, including the kidneys and bladder, is a poorly understood yet common disorder worldwide that leads to significant health care costs, morbidity, and work loss. Acetaminophen-induced liver damage is a major cause of death in patients with acute liver failure. Kidney and urinary stones and liver toxicity are disturbances linked to alterations in oxalate and sulfate homeostasis, respectively. The sulfate anion transporter–1 (Sat1; also known as Slc26a1) mediates epithelial transport of oxalate and sulfate, and its localization in the kidney, liver, and intestine suggests that it may play a role in oxalate and sulfate homeostasis. To determine the physiological roles of Sat1, we created Sat1−/− mice by gene disruption. These mice exhibited hyperoxaluria with hyperoxalemia, nephrocalcinosis, and calcium oxalate stones in their renal tubules and bladder. Sat1−/− mice also displayed hypersulfaturia, hyposulfatemia, and enhanced acetaminophen-induced liver toxicity. These data suggest that Sat1 regulates both oxalate and sulfate homeostasis and may be critical to the development of calcium oxalate urolithiasis and hepatotoxicity.

Introduction

Oxalate is a metabolic end product excreted into the urine (1), whereas sulfate (SO_4^{2-}) is highly reabsorbed by the kidneys (2, 3), playing important roles in many biochemical reactions. The regulation of oxalate and sulfate homeostasis is complex, with the kidney and liver playing critical roles. The sulfate anion transporter–1 (Sat1; ref. 4) is localized to the basolateral membrane of the renal proximal tubule (5) and the sinusoidal membrane of hepatocytes (6), where it mediates anion exchange (2, 7, 8). The human *SAT1* (9) and mouse *Sat1* (7) genes — also known as *SLC26A1* and *Slc26a1*, respectively — are located within exon 2/intron 2 (on the opposite strand) of the α-L-iduronidase (*IDUA*) gene (10). *IDUA* deficiency leads to mucopolysaccharidosis type I, a lysosomal storage disorder resulting from defective lysosomal degradation of glycosaminoglycans (11). Despite numerous studies characterizing Sat1 transport properties and tissue localization (2, 9, 12, 13), the physiological roles of Sat1 in vivo have not been resolved. To our knowledge, Sat1 has not been linked to any human disorders, and its role within the *IDUA* gene is unknown; therefore, we generated a *Sat1−/−* mouse by targeted disruption in order to characterize its functions in vivo. *Sat1−/−* mice showed perturbations in oxalate and sulfate homeostasis, leading to urolithiasis and hepatotoxicity, respectively.

Results

Sat1−/− mice. Our targeting strategy replaced *Sat1* exon 3 with a neomycin resistance (neo[R]) cassette (Figure 1A). Genomic Southern and PCR analyses confirmed deletion of *Sat1* in DNA from *Sat1−/−* mice (Figure 1, B–D). Genotypes of 303 mice were determined by PCR (Figure 1E): 86 were *Sat1+/+* (approximately 28%), 146 were *Sat1+/−* (approximately 48%), and 71 were *Sat1−/−* (approximately 24%), close to the Mendelian ratio of 1:2:1. This finding indicates that loss of Sat1 is not embryonic lethal. Because *Sat1* is localized within *Idua* (10), our targeting strategy was designed to selectively disrupt *Sat1* without

affecting *Idua* (Figure 1F). We confirmed this by determining that RT-PCR (using primers P6 and P7; Figure 1F and Supplemental Table 1; supplemental data available online with this article; doi:10.1172/JCI31474DS1) amplified similar amounts of *Idua* mRNA from kidney, liver, and ileum of *Sat1−/−* and *Sat1+/+* mice (data not shown). Idua enzyme activity in *Sat1−/−* liver (0.029 ± 0.003 nM/min/mg protein; $n = 3$) and kidney (0.015 ± 0.001 nM/min/mg protein; $n = 3$) were similar to that in *Sat1+/+* liver (0.025 to 0.050 nM/min/mg protein) and kidney (0.010 to 0.032 nM/min/mg protein), respectively (14), which suggests that loss of *Sat1* does not alter *Idua* function. No differences in body weight, tail length, or obvious distinguishing body features were observed in male and female *Sat1−/−* mice compared with *Sat1+/−* or *Sat1+/+* mice ($n = 15$–40 per group) from 1 to 24 weeks of age (data not shown). Gross histological analyses of the liver and brain, where Sat1 is normally expressed, showed no structural differences between *Sat1−/−* and *Sat1+/+* mice (data not shown).

A single 3.8-kb Sat1 transcript was detected in liver and kidney, but not ileum, of *Sat1+/+* and *Sat1+/−* mice, but not *Sat1−/−* mice (Figure 2B). Truncated cDNAs were amplified from *Sat1−/−* and *Sat1+/−* kidney mRNA (Figure 2C). Sequence analysis revealed Sat1 exons skipping from 2 to 4 (Figure 2A), with this cDNA lacking the first 587 bases of the Sat1 coding region, including the ATG start codon. Sat1 transcripts were amplified in the distal ileum, cecum, and proximal colon (Figure 2D). Sat1 protein was detected in basolateral membrane vesicles (BLMVs) from distal ileum, cecum, proximal colon (Figure 2E), and renal cortex (data not shown) of *Sat1+/+* mice, but not *Sat1−/−* mice. Oxalate and SO_4^{2-} transport was strongly reduced in BLMVs isolated from kidney, liver, distal ileum, cecum, and proximal colon of *Sat1−/−* mice compared with *Sat1+/+* mice (Table 1), with no differences observed in brush border membrane vesicles (BBMVs) of *Sat1+/+* and *Sat1−/−* mice (data not shown).

Role of Sat1 in the urinary system. *Sat1−/−* mice had infiltration of leukocytes around renal cortical vessels that was absent in *Sat1+/+* mice (Figure 3, A and B). Calcium oxalate crystals were observed in the lumen of kidney cortical tubules and the bladder of *Sat1−/−* mice, but not *Sat1+/+* mice (Figure 3, C–F). Crystals in the cortex and
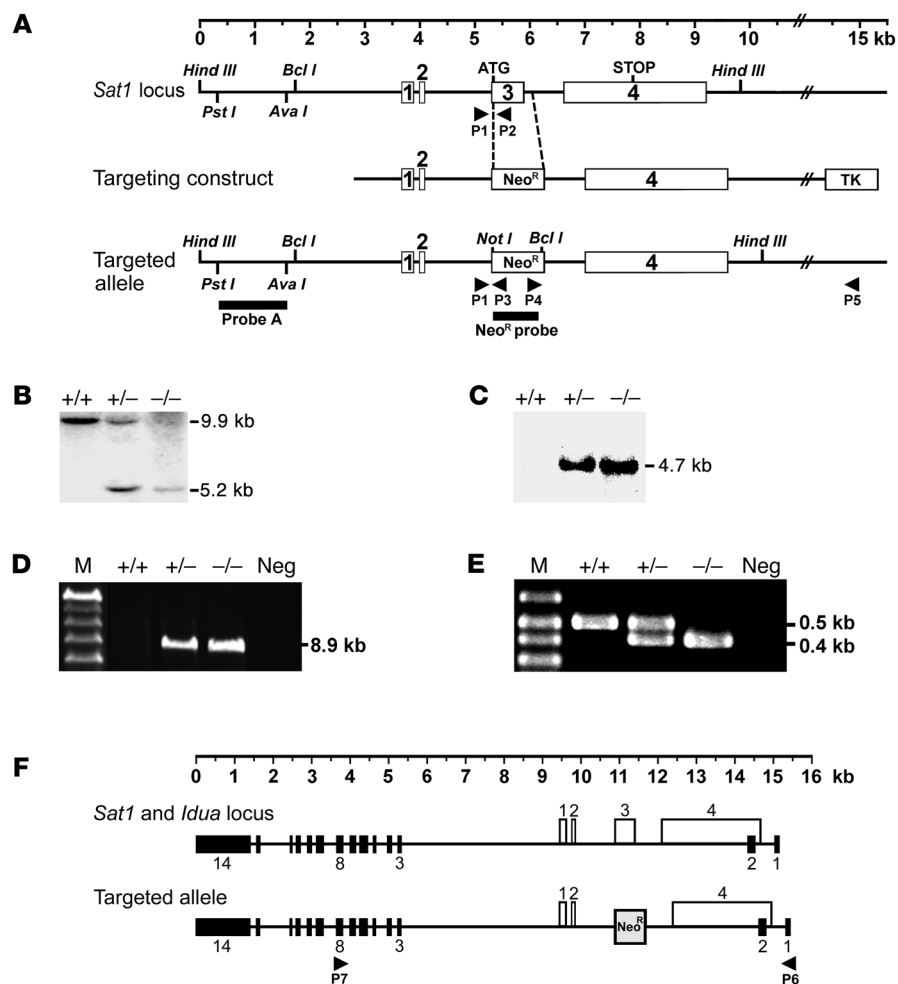
Figure 1
Targeted disruption of *Sat1*. (**A**) *Sat1* targeting strategy. Exons (boxes 1–4), restriction sites, probes, and primers P1–P5 are shown. Neo[R], neomycin resistance sequence; TK, thymidine kinase sequence. (**B**) Southern analysis of *Hind III*– and *Not I*–digested DNA from *Sat1+/+*, *Sat1+/−*, and *Sat1−/−* mice. Probe A detected 9.9-kb wild-type and 5.2-kb targeted allele fragments. (**C**) Southern analysis of *Bcl I*–digested DNA from *Sat1+/+*, *Sat1+/−*, and *Sat1−/−* mice. The neo[R] probe detected a single 4.7-kb fragment in *Sat1+/−* and *Sat1−/−* mice. (**D**) Forward (P4) and reverse (P5) primers amplified an 8.9-kb product in DNA samples from *Sat1+/−* and *Sat1−/−* mice. M, molecular mass ladder; Neg, negative control. (**E**) Primers P1 and P2 amplified a 0.5-kb wild-type fragment; P1 and P3 amplified a 0.4-kb targeted allele fragment. (**F**) Selective disruption of the *Sat1* gene located on the opposite strand within the *Idua* gene. *Sat1* exons (white boxes 1–4), *Idua* exons (black boxes 1–14), primers P6 and P7, and neomycin resistance sequence are shown.

outer medullary regions of the *Sat1−/−* kidney (Figure 4, A and B) were mainly composed of calcium, oxygen, and carbon (Figure 4C), indicating primary composition of calcium oxalate.

Role of Sat1 in the liver. Because sulfate is involved in detoxifying xenobiotics such as acetaminophen (APAP), and APAP administration causes rapid plasma sulfate depletion in humans and rodents (15, 16), we tested whether hepatic phase II sulfonation was affected in *Sat1−/−* mice. As shown previously in our *Nas1−/−* mice (17), 12-hour administration of 250 mg/kg APAP led to a 4-fold increase in serum alanine aminotransferase (ALT) in *Sat1−/−* mice compared with *Sat1+/+* mice (Figure 5A), and extensive liver necrosis was observed in *Sat1−/−* mice, but not *Sat1+/+* mice (Figure 5, C and D, and Supplemental Table 2). A single 250-mg/kg dose of APAP led to significantly greater reductions in glutathione (GSH) levels in *Sat1−/−* mice (reduced by approximately 96%) than in *Sat1+/+* mice (reduced by approxi-

mately 80%) after 2 hours; after 12 hours, basal GSH levels were restored in both *Sat1−/−* and *Sat1+/+* mice (Figure 5B).

Role of Sat1 in sulfate and oxalate homeostasis. Blood and urine profiling of *Sat1−/−* and *Sat1+/+* mice revealed that plasma oxalate levels increased by approximately 60%, whereas serum SO_4^{2-} levels were reduced by approximately 60%, in *Sat1−/−* mice compared with *Sat1+/+* mice (Table 2). Urine oxalate/creatinine and SO_4^{2-}/creatinine ratios and fractional excretion index (FEI) for SO_4^{2-} were significantly increased in *Sat1−/−* mice. Urinary glycolate/creatinine levels were not altered in *Sat1−/−* or *Sat1+/+* mice. A decrease in cecal oxalate and an increase in cecal sulfate content was observed in *Sat1−/−* mice.

Discussion

Overlapping genes in eukaryotes have been thought to be rare, but more recent analyses of the human and mouse genomes (18) suggest that overlapping transcripts in mammals may be more common
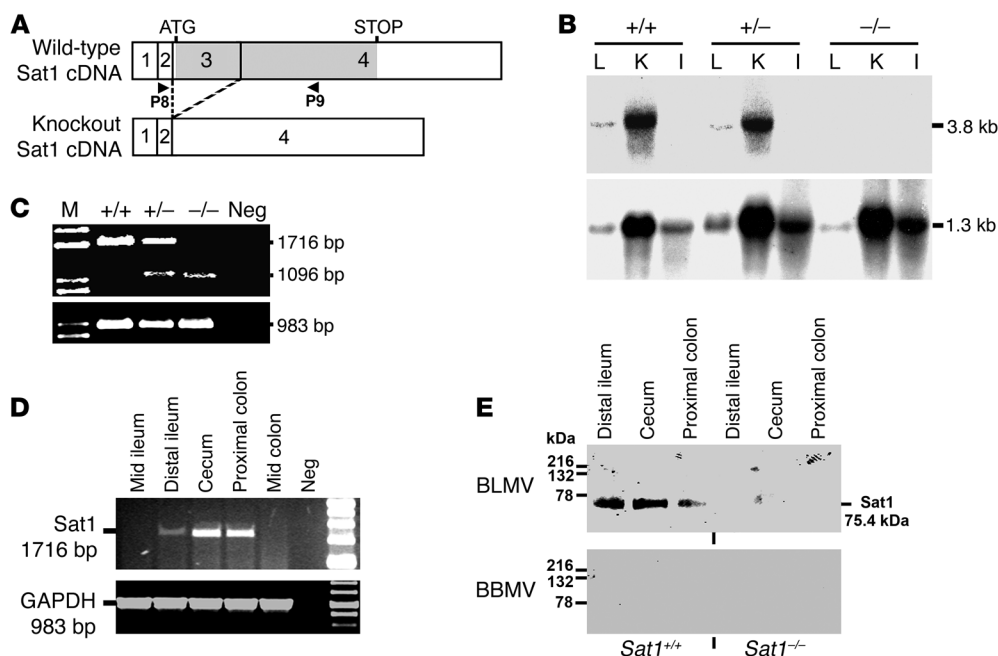
Figure 2

Analysis of Sat1 protein and mRNA. (**A**) Schematic of Sat1 cDNA and the predicted knockout cDNA lacking exon 3. Exons 1–4 (boxes), protein coding sequences (shading) of wild-type (3,821 nucleotides) and Sat1 knockout (3,201 nucleotides) cDNA, and primers P8 and P9 are shown. (**B**) Northern analysis of RNA from liver (L), kidney (K), and ileum (I) of $Sat1^{+/+}$, $Sat1^{+/-}$, and $Sat1^{-/-}$ mice. RNA was hybridized with a ^{32}P-labeled Sat1 cDNA (top), showing the 3.8-kb transcript, and GAPDH cDNA (bottom). (**C**) Total RNA from kidney was RT-PCR amplified. A 1,716-bp wild-type product and a 1,096-bp knockout Sat1 cDNA product (top) were amplified using primers P8 and P9. A 983-bp product (bottom) was amplified using GAPDH primers. (**D**) Total RNA from $Sat1^{+/+}$ intestinal segments was RT-PCR amplified. A 1,716-bp product was amplified using primers P8 and P9. A 983-bp product (bottom) was amplified using GAPDH primers. (**E**) Western analysis of protein from intestinal BLMVs and apical BBMVs. The Sat1 antibody detected a 75.4-kDa protein in $Sat1^{+/+}$ BLMVs, but not in $Sat1^{+/+}$ BBMVs or in $Sat1^{-/-}$ mice.

than previously thought. Early studies proposed that *Sat1* localization within the *Idua* gene may produce an antisense effect between the *Sat1* and *Idua* transcripts and act as a potential mechanism for coordinating expression of these genes (10). Selective disruption of *Idua* in mice showed no change in *Sat1* mRNA levels (14), and here we observed no change in the functional activity of *Idua* in tissues of *Sat1*$^{-/-}$ mice, which suggests that antisense effects are unlikely to play a significant role in regulating the expression of *Sat1* and *Idua* genes.

Urolithiasis is the most common chronic disorder of the urinary tract, with 70%–80% of stones being calcium oxalate crystals (19). Our observation of calcium oxalate crystals in the bladder and renal cortical and medullary tubules of *Sat1*$^{-/-}$ mice suggests that Sat1 plays a major role in renal oxalate excretion. Infiltration of leukocytes around renal cortical vessels of *Sat1*$^{-/-}$ mice suggests ureteral obstruction or obstructive uropathy (20). *Sat1*$^{-/-}$ mice had significantly elevated plasma oxalate levels, a greater than 2-fold increase in urine oxalate/creatinine ratio, no changes in urinary glycolate/creatinine levels (an indicator of hepatic oxalate production), and reduced oxalate transport in BLMVs of distal intestinal segments, which suggests that the hyperoxaluria in *Sat1*$^{-/-}$ mice arises most likely from hyperoxalemia rather than altered renal tubular oxalate handling. No changes were observed for whole blood pH; urine pH; urinary protein levels; cecal water content; serum levels of creatinine, Cl^-, PO_4^{2-}, Na^+, K^+, and Ca^{2+}; and FEIs of PO_4^{2-} and Ca^{2+} between *Sat1*$^{-/-}$ and *Sat1*$^{+/+}$ mice (Table 2), which suggests that homeostasis of these ions was not perturbed in *Sat1*$^{-/-}$ mice. *Sat1*$^{-/-}$ mice had significantly decreased serum sul-

fate levels, increased urine sulfate/creatinine, and increased FEI sulfate, suggesting that the hyposulfatemia in *Sat1*$^{-/-}$ mice most likely arises from increased renal excretion, as previously observed in *Nas1*$^{-/-}$ mice (21). This agrees with the present observation of strongly reduced sulfate transport across renal and liver BLMVs of *Sat1*$^{-/-}$ mice, which suggests that Sat1 is the predominant sulfate transporter on the renal proximal tubular basolateral and liver sinusoidal membranes. The hyposulfatemia and FEI sulfate values in *Sat1*$^{-/-}$ mice were comparable to those in *Nas1*$^{-/-}$ mice (21), which suggests that Sat1, together with NaS1, plays a crucial role

Table 1

BLMV transport of oxalate and sulfate

	$Sat1^{+/+}$	$Sat1^{-/-}$
Oxalate, pmol/mg protein/s		
Kidney	0.47 ± 0.07	0.06 ± 0.05
Liver	1.96 ± 0.07	0.97 ± 0.14
Distal ileum	0.59 ± 0.11	0.34 ± 0.09
Cecum	1.17 ± 0.09	0.62 ± 0.16
Proximal colon	1.06 ± 0.25	0.42 ± 0.08
Sulfate, pmol/mg protein/s		
Kidney	10.72 ± 1.28	0.59 ± 0.17
Liver	16.25 ± 1.74	2.57 ± 1.16

Results are mean ± SEM from BLMVs pooled from 10–15 mice.

Sat1$^{+/+}$ Sat1$^{-/-}$
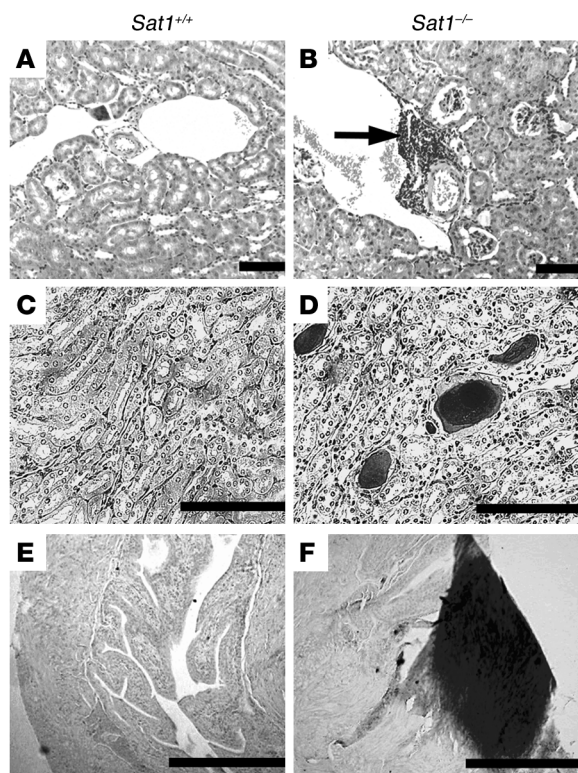
Figure 3
Urolithiasis in Sat1$^{-/-}$ mice. (**A** and **B**) Representative H&E-stained kidney sections showing infiltration of leukocytes (arrow) around the renal cortical vessels in 100% of Sat1$^{-/-}$ mice (n = 8), absent in Sat1$^{+/+}$ mice. (**C**–**F**) Representative Yasue-stained kidney (**C** and **D**) and bladder (**E** and **F**) sections showing calcium oxalate stones (dark staining) in kidney tubules of 47% Sat1$^{-/-}$ mice (n = 15) and bladders of 26% Sat1$^{-/-}$ mice (n = 19), but not in any Sat1$^{+/+}$ mice (n = 10). Gross histological analyses of additional tissues in which Sat1 is expressed (liver and brain) showed no structural differences between Sat1$^{-/-}$ and Sat1$^{+/+}$ mice (not shown). Scale bars: 100 μm (**A** and **B**); 500 μm (**C** and **D**); 2 mm (**E** and **F**).

in renal sulfate reabsorption and maintenance of serum sulfate levels. Despite Sat1 being expressed in several other tissues, including heart, brain, calvaria, and skeletal muscle (7), its role in these tissues — and to what degree these tissues contribute to circulating sulfate levels — is yet unknown. Our identification of Sat1 mRNA in the distal ileum, cecum, and proximal colon and Sat1 protein on the basolateral membrane of these intestinal segments suggests that Sat1 plays a role in distal intestinal oxalate and sulfate transport. This is corroborated with reduced oxalate transport in BLMVs from distal ileum, cecum, and proximal colon as well as decreased cecal oxalate content, indicating that the hyperoxalemia in Sat1$^{-/-}$ mice is most likely caused by reduced intestinal secretion of oxalate, as previously observed in Slc26a6$^{-/-}$ mice (22, 23). Our data suggest that Sat1 is the basolateral anion exchanger, which, together with Slc26a6 on the brush border membrane (22, 23), facilitates intestinal oxalate secretion.

Sulfate is required for detoxification of xenobiotics, including APAP (3), the leading cause of drug-related liver failure in humans (3, 24). Sat1$^{-/-}$ mice had increased APAP-induced liver toxicity, which suggests that the hyposulfatemia in Sat1$^{-/-}$ mice limits the supply of sulfate for APAP metabolism, as previously demonstrated in Nas1$^{-/-}$ mice (17). High doses of APAP cause rapid depletion of GSH, saturation of the sulfonation and glucuronidation pathways, and increased production and half-life of the toxic reactive intermediate N-acetyl-p-benzoquinone, which leads to cellular damage and death (25). Depletion of hepatic GSH levels and the rate of cellular GSH repletion are critical factors in APAP hepatotoxicity (26, 27). This agrees with our observations of decreased hepatic GSH levels and increased APAP-induced hepatotoxicity in Sat1$^{-/-}$ mice. The loss of Sat1 from the sinusoidal membranes of hepatocytes, where it facilitates sulfate import for sulfonation reactions (6), as well as the hyposulfatemia, exacerbate hepatic

sulfate depletion and drug-induced liver damage by drugs such as APAP. The roles of Sat1 polymorphisms (28) in drug metabolism rates are currently unknown, but the present study suggests that Sat1 may play an important role.

In conclusion, this is the first study to our knowledge to demonstrate Sat1 localization on the basolateral membrane of intestinal cells and show that loss of Sat1 expression leads to urinary stone formation and drug-induced hepatotoxicity, owing to altered homeostasis of oxalate and sulfate, respectively. Disturbed oxalate homeostasis led to hyperoxaluria with hyperoxalemia, nephrocalcinosis, and calcium oxalate urolithiasis, whereas perturbed sulfate homeostasis led to hyposulfatemia, hypersulfaturia, and enhanced hepatotoxicity in Sat1$^{-/-}$ mice. The present study provides an animal model for characterizing the etiology and mechanisms underlying calcium oxalate urolithiasis and the hepatic phase II sulfonation pathway and represents a therapeutic target for investigating human kidney stone formation and drug-induced hepatotoxicity in the general population.

Methods

Targeting vector construction. Fragments of Sat1 were PCR amplified and used to create the targeting vector shown in Figure 1A. A 2.3-kb fragment containing exons 1 and 2, and an 8.0-kb fragment containing exon 4, were subcloned on either side of the phosphoglycerate kinase–neo^R expression cassette of the pCAG Neo vector. Upon homologous recombination, this vector deleted approximately 0.9 kb of Sat1 genomic sequences, including the ATG start codon in exon 3 (Figure 2A).

Generation and identification of Sat1$^{-/-}$ mice. The targeting construct was electroporated into 129JSv mouse ES cells. Transfectants were selected for resistance to neomycin and ganciclovir (14). Individual clones that had undergone homologous recombination were identified by Southern blot analysis using an external 1.3-kb Pst I/Ava I fragment upstream of exon 1
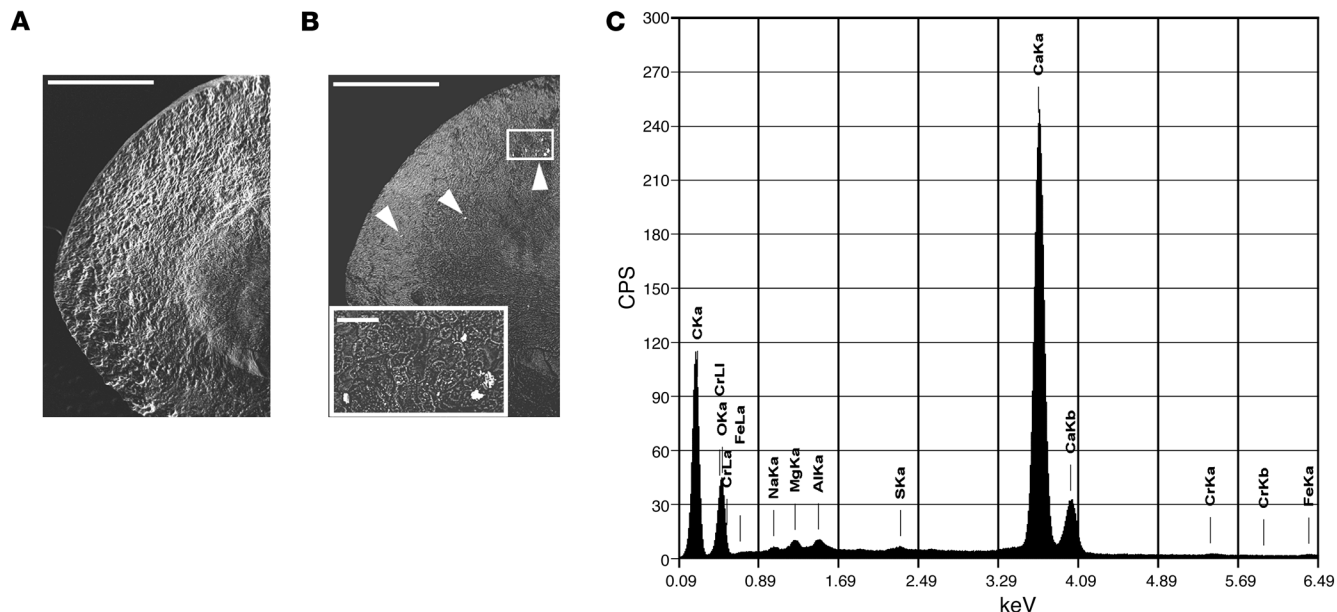
Figure 4
Energy dispersive X-ray spectrometry analysis of kidney stones in *Sat1*−/− mice. (**A** and **B**) Representative electron micrograph (**A**) and energy dispersive X-ray micrograph (**B**) showing kidney stones (arrowheads in **B**) in the renal cortex and outer medullary region of *Sat1*−/− mice. Higher-magnification view of the boxed region in **B** is shown in the inset. Scale bar: 1 mm; 100 μm (inset). (**C**) Elemental profile of kidney stones showing abundance of calcium (11.01% ± 0.03%), oxygen (36.53% ± 0.22%), and carbon (51.46% ± 0.08%), as well as trace levels (≤0.30%) of sodium, magnesium, aluminium, sulfur, chromium, and iron. CPS, counts per second; keV, kiloelectron volts.

as a probe (Figure 1A). Probe A detected a 9.9-kb *Hind III* wild-type allele fragment and a 5.2-kb *Hind III/Not I* recombinant allele fragment. Positive ES cell clones were injected into CD1 blastocysts that were implanted into foster mothers. Chimeric mice were bred with CD1 mice, and heterozygous offspring were intercrossed to produce *Sat1*−/− mice. Tail biopsies were further analyzed by Southern blotting using a neo^R probe (Figure 1A) and by using PCR to amplify an 8.9-kb recombinant allele fragment. PCR was performed using primer P4 in the neo^R gene cassette and antisense primer P5 downstream of exon 4 (Supplemental Table 1 and Figure 1A). Studies were performed on male mice with a mixed genetic background (129JSv and CD1). Mice were maintained on a 12-hour light/dark cycle and fed ad libitum on standard rodent chow (diet no. AIN93G; Glen Forrest Stockfeeders). All animal experiments were approved by the University of Queensland Anatomical Biosciences Ethics Committee.

Genotyping of mice. Mice were genotyped using primer P1 in intron 2 and antisense primer P3 in the neo^R gene cassette to PCR amplify a 0.4-kb fragment of the recombinant Sat1 allele (Supplemental Table 1 and Figure 1A). Primer P1 and antisense primer P2 in exon 3 were used to amplify a 0.5-kb fragment of the wild-type Sat1 allele (Supplemental Table 1 and Figure 1A). Cycle parameters were as follows: 95°C for 10 seconds followed by 35 cycles of 95°C for 10 seconds, 58°C for 30 seconds, and 68°C for 3 minutes.

Analysis of RNA. Total RNA (10 μg) was separated on a 1.2% agarose formaldehyde gel in MOPS buffer and transferred to Hybond-XL nylon membranes (Amersham). The blots were probed with a 1.4-kb Sat1 cDNA and a 0.6-kb mouse GAPDH cDNA probe. For RT-PCR, total RNA (2 μg) was reverse transcribed using random hexamers and Moloney Murine Leukemia Virus reverse transcriptase (Progen), as recommended by the manufacturer. Primer P8 in exon 2 and antisense primer P9 in exon 4 (Figure 2A and Supplemental Table 1) were used to amplify Sat1 cDNA fragments. GAPDH cDNAs were RT-PCR amplified using established primer sequences (17).

Figure 5
Increased hepatotoxicity in *Sat1*−/− mice. (**A** and **B**) Serum ALT and liver GSH levels in *Sat1*+/+ (white bars) and *Sat1*−/− (black bars) mice 0, 2, and 12 hours after administration of 250 mg/kg APAP. Results are mean ± SEM (n = 4–8 per group). *P < 0.05 versus time 0 *Sat1*+/+; #P < 0.05 versus time 0 *Sat1*−/−. (**C** and **D**) Representative H&E-stained liver sections of *Sat1*+/+ and *Sat1*−/− mice (n = 6–7 per group) 12 hours after administration of 250 mg/kg APAP, showing liver necrosis in *Sat1*−/− mice. Scale bars: 100 μm.

Table 2
Blood, urinary, and cecal profiles of *Sat1⁺/⁺* and *Sat1⁻/⁻* mice

	$Sat1^{+/+}$ (n)	$Sat1^{-/-}$ (n)
Plasma		
Oxalate, μM	8.1 ± 0.8 (12)	13.0 ± 1.0 (10)[C]
Serum		
SO_4^{2-}, mM	0.64 ± 0.02 (10)	0.27 ± 0.03 (8)[D]
Cl^-, mM	114.1 ± 1.1 (8)	115.9 ± 1.5 (8)
PO_4^{2-}, mM	2.54 ± 0.14 (8)	2.73 ± 0.15 (8)
Na^+, mM	145.0 ± 1.9 (5)	144.8 ± 0.5 (5)
K^+, mM	6.1 ± 0.9 (5)	6.3 ± 0.7 (5)
Ca^{2+}, mM	2.34 ± 0.02 (8)	2.34 ± 0.01 (8)
Creatinine, μM	16.7 ± 1.1 (7)	15.5 ± 0.7 (7)
Whole blood		
pH	7.34 ± 0.02 (8)	7.35 ± 0.02 (8)
Urine		
Oxalate/creatinine[A]	0.33 ± 0.05 (11)	0.69 ± 0.08 (8)[E]
SO_4^{2-}/creatinine[A]	10.44 ± 0.56 (5)	12.07 ± 0.30 (6)[E]
Ca^{2+}/creatinine[A]	0.27 ± 0.09 (7)	0.20 ± 0.08 (7)
Glycolate/creatinine[A]	0.18 ± 0.02 (9)	0.18 ± 0.03 (9)
Cl^-/creatinine[A]	25.28 ± 11.26 (3)	28.75 ± 5.76 (5)
PO_4^{2-}/creatinine[A]	10.32 ± 2.73 (7)	10.29 ± 2.58 (7)
Total protein, ng/μl	2.07 ± 0.81 (10)	1.37 ± 0.77 (10)
Creatinine, mM	3.28 ± 0.27 (11)	3.73 ± 0.31 (8)
pH	7.24 ± 0.17 (8)	6.99 ± 0.28 (8)
FEI[B]		
SO_4^{2-}	0.38 ± 0.03 (5)	0.96 ± 0.12 (6)[D]
Ca^{2+}	0.021 ± 0.007 (7)	0.020 ± 0.008 (7)
PO_4^{2-}	0.079 ± 0.024 (7)	0.080 ± 0.023 (7)
Cecal		
Oxalate, μmol/g	18.6 ± 2.2 (11)	12.7 ± 1.1 (11)[E]
SO_4^{2-}, μmol/g	10.7 ± 1.2 (11)	15.1 ± 1.2 (11)[E]
H_2O, %	66.8 ± 2.5 (13)	67.9 ± 1.5 (14)

Results are mean ± SEM. [A]Molar ratio. [B]Ratio between [serum or plasma creatinine × (urine SO_4^{2-}, PO_4^{2-}, or Ca^{2+})] and [urine creatinine × (serum or plasma SO_4^{2-}, PO_4^{2-}, or Ca^{2+})]; all measurements in mM. [C]$P < 0.001$; [D]$P < 0.0001$; [E]$P < 0.05$ versus *Sat1⁺/⁺*.

tography with suppressed conductivity detection using a Dionex ICS2000 running Chromeleon 6.80 (32, 33). Upon collection of 100 μl serum and urine, 10 μl HCl (8M) was quickly added, and the samples were frozen at –80°C to prevent oxalate precipitation and oxalogenesis. Serum and urine creatinine levels were quantitated enzymatically using a Vitros 5.1 FS chemistry analyzer (Ortho-Clinical Diagnostics). Serum PO_4^{2-}, Na^+, K^+, Cl^-, Ca^{2+}, and ALT concentrations were assayed by a commercial pathology laboratory (Sullivan Nicolaides Pathology) using a Vitros 250 chemistry analyzer (Ortho-Clinical Diagnostics). Urinary glycolate levels were quantitated using an Agilent 6890 GC and 5973A MSD running MSD Chemstation B.01.00. Urine total protein levels were quantitated using a protein microassay kit (BioRad). Whole blood and urine pH was measured with an ISFET pH meter (Shindengen). Hepatic GSH levels were assayed using a commercially available kit (Cayman Chemical Co.). H_2O content of cecal samples was determined by weighing samples before and after they were desiccated under vacuum for 30 hours at 25°C. Kidney and liver IDUA activity was measured using a fluorometric assay (34).

Histopathological analysis. Tissues were dissected into approximately 50 volumes of 10% buffered formalin and fixed for 3 days prior to paraffin embedding. Embedded tissue was sectioned, stained with H&E or by the Yasue histochemical method (35) for detecting calcium oxalate crystals, and examined by light microscopy. Liver sections were scored blinded to genotype for the severity of degeneration and necrosis using a 0–5 scale as previously described (36).

APAP administration. APAP (Sigma-Aldrich) was dissolved in saline and filter-sterilized. At approximately 3 months of age, mice received i.p. injection of a 250-mg/kg dose of APAP (n = 4–8 per group). Mice were sacrificed at 2 or 12 hours after APAP administration.

Statistics. Statistical significance between *Sat1⁺/⁺* and *Sat1⁻/⁻* or *Sat1⁺/⁻* groups was assessed using an unpaired Student's 2-tailed *t* test. Statistical significance between *Sat1⁺/⁺* and *Sat1⁻/⁻* groups with respective controls at time point 0 was evaluated using 1-way ANOVA followed by Duncan's multiple range test. Differences in histology scores were analyzed by the Mann-Whitney test. In all cases, a *P* value less than 0.05 was considered significant.

Membrane vesicle preparation, transport studies, and Western blotting. BLMVs and BBMVs were isolated from mouse kidney, liver, and intestine using previously described methods (29, 30). Vesicles were preincubated in buffer containing 120 mM potassium gluconate, 30 mM KCl, and 15 mM HEPES pH 8.2 for 2 hours at 20°C. The uptakes of SO_4^{2-} (0.1 mM) and oxalate (20 μM), each performed in quadruplicate, were measured at 10 seconds (SO_4^{2-}) and 30 seconds (oxalate) in media containing 150 mM potassium gluconate and 15 mM HEPES, pH 8.2, by the rapid filtration technique (23, 31). BLMV protein (5 μg) was separated on a 10% SDS polyacrylamide gel and transferred to nylon membrane (Immobilon-FL membrane; Millipore). Sat1 proteins were detected with a Sat1 antibody (5) provided by L.P. Karniski (University of Iowa, Iowa City), with IRDye CW800-labeled anti-mouse IgG (diluted 1:20,000) and the Odyssey Imaging System (LI-COR Biotechnology). All experiments were repeated at least twice.

Biochemical analyses. Mouse blood was collected from the submandibular vein using an animal bleeding lancet (MEDIpoint Inc.). Single urine samples were collected upon spontaneous micturition during mouse handling, prior to blood collection. A turbidimetric assay was used to measure free sulfate levels (17). Oxalate was measured by ion chroma-

Address correspondence to: Daniel Markovich, School of Biomedical Sciences, University of Queensland, St. Lucia, Queensland 4072, Australia. Phone: 61.7.3365.1400; Fax: 61.7.3365.1766; E-mail: d.markovich@uq.edu.au.

1. Greger R, Lang F, Oberleithner H, Deetjen P. Handling of oxalate by the rat kidney. *Pflugers Arch.* 1978;374(3):243–248.

2. Markovich D. Physiological roles and regulation of mammalian sulfate transporters. *Physiol Rev.* 2001;81(4):1499–1533.

3. Falany CN. Enzymology of human cytosolic sulfotransferases. *FASEB J.* 1997;11(4):206–216.

4. Bissig M, Hagenbuch B, Stieger B, Koller T, Meier PJ. Functional expression cloning of the canalicular sulfate transport system of rat hepatocytes. *J Biol Chem.* 1994;269(4):3017–3021.

5. Karniski LP, Lotscher M, Fucentese M, Hilfiker H, Biber J, Murer H. Immunolocalization of sat-1 sulfate/oxalate/bicarbonate anion exchanger in the rat kidney. *Am J Physiol.* 1998;275(1 Pt 2):F79–F87.

6. Quondamatteo F, et al. Localization of the sulfate/anion exchanger in the rat liver. *Am J Physiol Gastrointest Liver Physiol.* 2006;290(5):G1075–G1081.

7. Lee A, Beck L, Markovich D. The mouse sulfate anion transporter gene Sat1 (Slc26a1): cloning, tissue distribution, gene structure, functional characterization, and transcriptional regulation thyroid hormone. *DNA Cell Biol.* 2003;22(1):19–31.

8. Markovich D, Aronson PS. Specificity and regulation of renal sulfate transporters. *Annu Rev Physiol.* 2007;69:361–375.

9. Regeer RR, Lee A, Markovich D. Characterization of the human sulfate anion transporter (hsat-1) protein and gene (SAT1; SLC26A1). *DNA Cell Biol.* 2003;22(2):107–117.

10. Clarke LA, et al. Murine alpha-L-iduronidase: cDNA isolation and expression. *Genomics.* 1994;24(2):311–316.

11. Neufeld EF, Muenzer J. The mucopolysaccharidoses. In: Scriver CR, Beaudet AL, Sly WS, and Valle D, eds. *The Metabolic Basis of Inherited Disease.* New York, NY: McGraw-Hill; 1994:2465–2498.

12. Lee A, Dawson PA, Markovich D. NaSi-1 and Sat-1: Structure, function and transcriptional regulation of two genes encoding renal proximal tubular sulfate transporters. *Int J Biochem Cell Biol.* 2005;37(7):1350–1356.

13. Mount DB, Romero MF. The SLC26 gene family of multifunctional anion exchangers. *Pflugers Arch.* 2004;447(5):710–721.

14. Clarke LA, et al. Murine mucopolysaccharidosis type I: targeted disruption of the murine alpha-L-iduronidase gene. *Hum Mol Genet.* 1997;6(4):503–511.

15. Morris ME, Levy G. Serum concentration and renal excretion by normal adults of inorganic sulfate after acetaminophen, ascorbic acid, or sodium sulfate. *Clin Pharmacol Ther.* 1983;33(4):529–536.

16. Kim H, Rozman P, Madhu C, Klaassen C. Homeostasis of sulfate and 3′-phosphoadenosine 5′-phosphosulfate in rats after acetaminophen administration. *J Pharmacol Exp Ther.* 1992;261(3):1015–1021.

17. Lee S, Dawson PA, Hewavitharana AK, Shaw PN, Markovich D. Disruption of NaS1 sulfate transport function in mice leads to enhanced acetaminophen-induced hepatotoxicity. *Hepatology.* 2006;43(6):1241–1247.

18. Veeramachaneni V, Makalowski W, Galdzicki M, Sood R, Makalowska I. Mammalian overlapping genes: the comparative perspective. *Genome Res.* 2004;14(2):280–286.

19. Asplin JR. Hyperoxaluric calcium nephrolithiasis. *Endocrinol Metab Clin North Am.* 2002;31(4):927–949.

20. Schreiner GF, Harris KP, Purkerson ML, Klahr S. Immunological aspects of acute ureteral obstruction: immune cell infiltrate in the kidney. *Kidney Int.* 1988;34(4):487–493.

21. Dawson PA, Beck L, Markovich D. Hyposulfatemia, growth retardation, reduced fertility and seizures in mice lacking a functional NaSi-1 gene. *Proc Natl Acad Sci U S A.* 2003;100(23):13704–13709.

22. Wang Z, et al. Renal and intestinal transport defects in Slc26a6-null mice. *Am J Physiol Cell Physiol.* 2005;288:C957–C965.

23. Jiang Z, et al. Calcium oxalate urolithiasis in mice lacking anion transporter Slc26a6. *Nat Genet.* 2006;38(4):474–478.

24. Gill RQ, Sterling RK. Acute liver failure. *J Clin Gastroenterol.* 2001;33(3):191–198.

25. Mitchell J, Jollow D, Potter W, Davis D, Gillette J, Brodie B. Acetaminophen-induced hepatic necrosis. I. Role of drug metabolism. *J Pharmacol Exp Ther.* 1973;187(1):185–194.

26. DeLeve LD, Kaplowitz N. Glutathione metabolism and its role in hepatotoxicity. *Pharmacol Ther.* 1991;52(3):287–305.

27. Henderson CJ, Wolf CR, Kitteringham N, Powell H, Otto D, Park BK. Increased resistance to acetaminophen hepatotoxicity in mice lacking glutathione S-transferase Pi. *Proc Natl Acad Sci U S A.* 2000;97(23):12741–12745.

28. Dawson P, Markovich D. Genetic polymorphisms of human sulfate transporters. *Curr Pharmacogenomics.* 2007;5:262–274.

29. Hilden SA, Johns CA, Guggino WB, Madias NE. Techniques for isolation of brush-border and basolateral membrane vesicles from dog kidney cortex. *Biochim Biophys Acta.* 1989;983(1):77–81.

30. Meier PJ, Sztul ES, Reuben A, Boyer JL. Structural and functional polarity of canalicular and basolateral plasma membrane vesicles isolated in high yield from rat liver. *J Cell Biol.* 1984;98(3):991–1000.

31. Tenenhouse HS, Scriver CR. The defect in transcellular transport of phosphate in the nephron is located in brush-border membranes in X-linked hypophosphatemia (Hyp mouse model). *Can J Biochem.* 1978;56(6):640–646.

32. McWhinney BC, Cowley DM, Chalmers AH. Simplified column liquid chromatographic method for measuring urinary oxalate. *J Chromatogr.* 1986;383(1):137–141.

33. Palgi N, Vatnick I, Pinshow B. Oxalate, calcium and ash intake and excretion balances in fat sand rats (Psammomys obesus) feeding on two different diets. *Comp Biochem Physiol A Mol Integr Physiol.* 2005;141(1):48–53.

34. Hopwood JJ, Muller V, Smithson A, Baggett N. A fluorometric assay using 4-methylumbelliferyl alpha-L-iduronide for the estimation of alpha-L-iduronidase activity and the detection of Hurler and Scheie syndromes. *Clin Chim Acta.* 1979;92(2):257–265.

35. Yasue T. Histochemical identification of calcium oxalate. *Acta Histochem Cytochem.* 1969;2:83–95.

36. Manautou JE, Silva VM, Hennig GE, Whiteley HE. Repeated dosing with the peroxisome proliferator clofibrate decreases the toxicity of model hepatotoxic agents in male mice. *Toxicology.* 1998;127(1–3):1–10.